

# Selective Incorporation of Iron Sites into MFI Zeolite Framework by One-Pot Synthesis

Published as part of a *Crystal Growth and Design* virtual special issue on Zeolite Crystal Engineering

Xunming Su, Zhong-Pan Hu, Jingfeng Han, Yingxu Wei,\* and Zhongmin Liu\*



Cite This: *Cryst. Growth Des.* 2023, 23, 2644–2651



Read Online

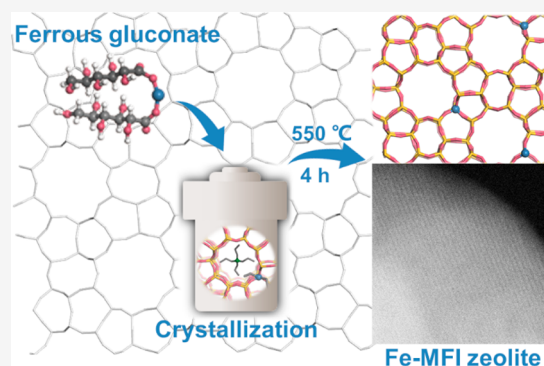
ACCESS |

Metrics & More

Article Recommendations

Supporting Information

**ABSTRACT:** Developing highly efficient methods to selectively incorporate active metal sites into the zeolite framework is crucial for the large-scale utilization of metal-zeolites in various catalytic reactions including alkane conversion. Herein, ferrous gluconate is developed as an efficient metal precursor to embed Fe atoms into the MFI siliceous zeolite framework. The crystallization time and Si/Fe ratio are systematically investigated. It is revealed that the ferrous gluconate is well soluble and stable under alkaline conditions, allowing ferrous gluconate to participate in the whole crystallization course of zeolite. Multiple characterizations demonstrate that the tetrahedrally coordinated Fe atoms are selectively incorporated into the MFI siliceous zeolite framework (Fe-MFI). A catalytic test in propane dehydrogenation shows that the optimized Fe-MFI zeolite possesses high activity, propylene selectivity, and durability. This study opens an efficient strategy to incorporate isolated Fe atoms into the zeolite framework.



## INTRODUCTION

The incorporation of metal active sites into porous materials is widely applied in industrial catalysis, energy conversion, and environmental treatment.<sup>1–6</sup> In particular, metal-zeolite materials have become one of the most efficient catalysts since they depend on both the structure of the active sites and the surrounding microenvironment. Indeed, possessing good thermal stability, tunable acidity, and confined nanospace, metal-zeolite materials can provide a satisfactory reaction environment for reactant conversion.<sup>7–10</sup> Through the synergistic effect of active metal sites and the reaction environment, the metal-zeolite can efficiently perform the tasks of adsorption and activation of reactants as well as the generation and desorption of products.<sup>11–13</sup>

In recent years, researchers have been very enthusiastic about designing different types of metal-zeolites.<sup>14–20</sup> Due to the nontoxicity and high activity, Fe species are often introduced into zeolite for various catalytic reactions such as CH<sub>4</sub> oxidation to CH<sub>3</sub>OH, ammonia decomposition, oxidation of benzene to phenol by NO, and propane dehydrogenation (PDH).<sup>21–27</sup> In the PDH process, the activation of the C(sp<sup>3</sup>)–H bond of propane as the first step is very challenging in reaction. Because of the high endothermicity of propane dehydrogenation, a reaction temperature >500 °C is needed to achieve a feasible propane conversion.<sup>28</sup> Satisfyingly, the unique microenvironment of zeolites can modify the electronic and geometric properties of Fe species, making Fe-based zeolites particularly beneficial for

propane dehydrogenation.<sup>29,30</sup> In general, many kinds of Fe species would be formed on zeolites, including tetrahedral or octahedral coordinated Fe sites embedded into the zeolite framework and small Fe<sub>x</sub>O<sub>y</sub> oligomers or iron oxide nanoparticles loaded into the zeolite channels or onto the zeolite surface.<sup>13,31–38</sup>

The preparation methods can affect the type of Fe species and their distribution within the zeolite. For example, the introduction of Fe ions into HZSM-5 zeolite by the postsynthesis methods (e.g., incipient wetness impregnation, ions exchange, and chemical vapor deposition of volatile iron compounds) results in Fe ions entering into the zeolite channel, forming isolated ferrous ions and octahedral coordinated ferric ions at the Brønsted acid sites of the ZSM-5 zeolite channel, which exhibits interesting catalytic performance.<sup>39–44</sup> However, iron oxide nanoparticles (Fe<sub>2</sub>O<sub>3</sub>, Fe<sub>3</sub>O<sub>4</sub>, etc.) would be inevitably formed on the zeolite surface during these synthesis processes, which would lead to some undesired performance such as low selectivity and quick deactivation.<sup>31,45</sup> Therefore, many other methods have been

**Received:** December 13, 2022

**Revised:** March 3, 2023

**Published:** March 13, 2023



exploited to incorporate Fe species into the zeolite framework, such as the improved postsynthesis and hydrothermal synthesis methods. Lobo and co-workers prepared Fe-based zeolites by hydrothermal synthesis method using  $\text{Fe}_2(\text{SO}_4)_3$  as a metal precursor, exhibiting high selectivity and low activation energies as compared with those for [Al]ZSM-5 catalysts in propane dehydrogenation.<sup>46,47</sup> However, the framework Fe species would migrate to extra-framework positions during the calcination process, which is negative for alkane dehydrogenation. Recently, Zhang et al. prepared Fe-S-1 zeolite by the hydrothermal synthesis method, and the characterization results illustrated that isolated Fe atoms and iron oxide clusters or nanoparticles could be simultaneously formed over the Fe-S-1 zeolite during the crystallization process owing to the low stability of Fe ions under alkaline synthesis conditions.<sup>48</sup> To overcome this issue, Xiao and co-workers synthesized Fe-containing MFI siliceous zeolite (FeS-1-EDTA) using ethylenediaminetetraacetic sodium as a metal chelating agent. Owing to the strong coordination between EDTA and Fe ions, isolated Fe species can be efficiently introduced into the FeS-1-EDTA zeolite framework without iron oxide clusters or nanoparticles. Ethane dehydrogenation results showed that the isolated Fe species incorporated into the MFI framework could facilitate the cleavage of the C–H bond, weaken the sorption of ethene, and thereby hinder the coke formation.<sup>49</sup> Therefore, it is of great meaning to exploit a good approach for selectively embedding Fe sites into the zeolite framework. Recently, the isolated metal sites were successfully synthesized onto  $\text{SiO}_2$  and  $\text{Al}_2\text{O}_3$  supports via organometallic precursors (e.g., diethylzinc, bis(2,4-dimethyl-1,3-pentadienide), iron(II), and  $(\equiv\text{SiO})_2\text{V}^{\text{V}}(\text{O})\text{Mes}$  (Mes = 2,4,6-trimethylphenyl)).<sup>50–52</sup>

Herein, ferrous gluconate is exploited as a metal precursor to introduce Fe sites into the MFI siliceous zeolite framework (Fe-MFI). The UV–vis spectra demonstrate that ferrous gluconate can efficiently incorporate Fe atoms into the MFI framework. The crystallization processes of Fe-MFI at different times are investigated and reveal that the ferrous gluconate is involved in the whole crystallization course. Furthermore, multiple characterizations are performed to demonstrate the structural and chemical properties of Fe-MFI zeolite. The prepared Fe-MFI zeolites have good crystallinity and high dispersion of Fe sites, which exhibit high propane dehydrogenation.

## ■ EXPERIMENTAL SECTION

**Chemicals and Materials.** Tetraethylorthosilicate (TEOS, Xilong Scientific Co., Ltd.), tetrapropylammonium hydroxide solution (TPAOH, 25%, Sinopharm Chemical Reagent Co., Ltd.), ferrous gluconate hydrate ( $\text{Fe}(\text{C}_6\text{H}_{12}\text{O}_7)_2$ , 98%, Shanghai Aladdin Biochemical Technology Co., Ltd.), ferric nitrate ( $\text{Fe}(\text{NO}_3)_3 \cdot 9\text{H}_2\text{O}$ , 98%, Shanghai Aladdin Biochemical Technology Co., Ltd.), ferrous oxalate ( $\text{FeC}_2\text{O}_4 \cdot 2\text{H}_2\text{O}$ , 98%, Shanghai Aladdin Biochemical Technology Co., Ltd.), deionized (DI) water were used.

**Synthesis of Fe-Based Zeolites.** Ferrous gluconate was used as a metal precursor to embed Fe species into the Fe-based zeolites.  $\text{Fe}(\text{C}_6\text{H}_{12}\text{O}_7)_2$  was added to crystallized gels containing tetraethylorthosilicate (TEOS), tetrapropylammonium hydroxide (TPAOH), and deionized (DI) water. Typically, Fe-MFI zeolites were prepared by the one-pot synthesis method. The clear synthesis gel with the component of  $1.0\text{SiO}_2/0.4\text{TPAOH}/35\text{H}_2\text{O}/a\text{Fe}(\text{C}_6\text{H}_{12}\text{O}_7)_2$  ( $a = 0.011, 0.019$ , and  $0.034$ ) was transferred into a Teflon-lined, stainless steel autoclave and heated statically at  $170\text{ }^\circ\text{C}$  for 72 h and then calcined in the air at  $550\text{ }^\circ\text{C}$  for 4 h with a heating rate of  $1.5\text{ }^\circ\text{C min}^{-1}$ . For comparison, we also synthesized Fe-zeolites by direct addition of ferric nitrate ( $\text{Fe}(\text{NO}_3)_3 \cdot 9\text{H}_2\text{O}$ ) and ferrous oxalate

( $\text{FeC}_2\text{O}_4 \cdot 2\text{H}_2\text{O}$ ), denoted as FeN-MFI and FeC-MFI zeolites, respectively.

**Characterizations.** Powder X-ray diffraction (XRD) patterns were carried out on a PANalytical X'Pert Pro X-ray diffractometer. A Philips Magix-601 X-ray fluorescence (XRF) spectrometer measured the inclusion of elemental compositions in the samples. The porosities of the zeolites were measured by  $\text{N}_2$  sorption at  $-196\text{ }^\circ\text{C}$  on a Micromeritics ASAP2020 volumetric adsorption analyzer. Before the measurement, all the samples were degassed at  $350\text{ }^\circ\text{C}$  under a vacuum for 4 h. The total specific surface area was evaluated based on the Brunauer–Emmett–Teller (BET) equation. The crystal morphology of Fe-MFI zeolite was observed by a scanning electron microscope (SEM, Hitachi SU8020). High-resolution  $\text{C}_s$ -corrected HAADF-STEM (HAADF-STEM) images and EDS elemental mapping images were collected on a JEM-ARM200F transmission electron microscope. Ultraviolet–visible spectrophotometer (UV–vis) spectra were detected at room temperature using a Shimadzu MV2450V. X-ray photoelectron spectroscopy (XPS) was performed using an ESCALAB 250Xi spectrometer. The binding energy of C 1s at  $284.6\text{ eV}$  was used as the reference. Fourier transform infrared spectra of pyridine (Py-FTIR) analysis was recorded in Bruker Optics XF808-04 instrument with a mercury cadmium telluride (MCT) detector. The 20 mg samples were pressed into a self-supporting disc and placed into a quartz cell. Afterward, the samples were pretreated at  $400\text{ }^\circ\text{C}$  for 60 min under He atmosphere and then cooled to room temperature. Subsequently,  $2\text{ }\mu\text{L}$  of pyridine was injected, followed by purging with He for 30 min to remove physisorbed pyridine. Ammonium temperature-programmed desorption ( $\text{NH}_3$ -TPD) profiles and  $\text{H}_2$  temperature-programmed reduction ( $\text{H}_2$ -TPR) tests were measured by AutoChem II 2910. Thermal gravimetric analyses (TG/DTA) were carried out on the NETZSCH ATS 499 F3 analyzer from  $25$  to  $800\text{ }^\circ\text{C}$  with a heating speed of  $10\text{ }^\circ\text{C min}^{-1}$  under the airflow of  $20\text{ mL min}^{-1}$ . Propylene temperature-programmed desorption ( $\text{C}_3\text{H}_6$ -TPD) tests were performed in a fixed micro-reactor equipped with a mass spectrometer (Shimadzu MS-QP2010 SE). Typically,  $0.2\text{ g}$  sample was pretreated in  $\text{H}_2$  flowing ( $20\text{ mL min}^{-1}$ ) at  $580\text{ }^\circ\text{C}$  for 1 h and then purged in Ar flowing ( $20\text{ mL min}^{-1}$ ) for 30 min. After cooling down to  $100\text{ }^\circ\text{C}$ ,  $5\%\text{C}_3\text{H}_6/\text{Ar}$  ( $20\text{ mL min}^{-1}$ ) was passed through the pretreated catalysts for 30 min and then purged in Ar flowing ( $20\text{ mL min}^{-1}$ ). Until the baseline flat, the adsorbed sample was heated to the desired temperature with a heating rate of  $10\text{ }^\circ\text{C min}^{-1}$ . The desorbed products (i.e.,  $\text{H}_2$ ,  $\text{C}_2\text{H}_4$ ,  $\text{C}_2\text{H}_6$ ,  $\text{C}_3\text{H}_6$ , and  $\text{C}_3\text{H}_8$ ) were measured by an online MS.

**Catalytic Activity Measurement.** The propane dehydrogenation reaction was carried out in a quartz tubular fixed-bed reactor at  $600\text{ }^\circ\text{C}$  under atmospheric pressure. Catalysts ( $0.2\text{ g}$ ,  $20\text{--}40$  mesh) were activated in situ in Ar flow of  $20\text{ mL min}^{-1}$  at  $600\text{ }^\circ\text{C}$  for 1 h and then treated in  $\text{H}_2$  flowing ( $20\text{ mL min}^{-1}$ ) for 1 h. After purifying by Ar,  $5\%\text{C}_3\text{H}_8/\text{Ar}$  ( $20\text{ mL min}^{-1}$ ) was passed into the reactor. An online gas chromatograph equipped with a flame ionization detector (FID) and a thermal conductivity detector was used to analyze the reaction products.  $\text{C}_3\text{H}_8$  conversion ( $C_{\text{propane}}$ ) and  $\text{C}_3\text{H}_6$  selectivity ( $S_{\text{propylene}}$ ) were calculated according to the following two equations:

$$C_{\text{propane}} = \frac{\sum n_x C_x - n_x C_{\text{C}_3\text{H}_8}}{\sum n_x C_x} \times 100 \quad (1)$$

$$S_{\text{propylene}} = \frac{n_x C_x}{\sum n_x C_x - n_x C_{\text{C}_3\text{H}_8}} \times 100 \quad (2)$$

where  $x$  is the products in the effluent gas flow (i.e.,  $\text{CH}_4$ ,  $\text{C}_2\text{H}_4$ ,  $\text{C}_2\text{H}_6$ , and  $\text{C}_3\text{H}_6$ ),  $n_x$  is the carbon atoms of products  $x$ , and  $C_x$  is the corrected mole concentration of product  $x$ .

## ■ RESULTS AND DISCUSSION

Figure 1a shows the powder XRD patterns of all zeolites with diffraction peaks appearing at  $2\theta = 7.9^\circ$ ,  $8.8^\circ$ ,  $23.1^\circ$ ,  $23.9^\circ$ , and  $24.4^\circ$ , which are typical MFI zeolite structures. Moreover, no characteristic peaks associated with  $\text{Fe}_2\text{O}_3$  are observed,

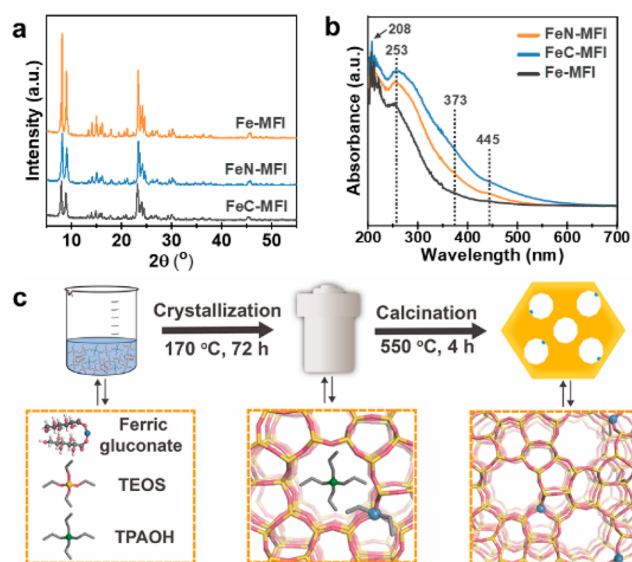


**Figure 1.** (a) XRD patterns of Fe-MFI, FeN-MFI, and FeC-MFI zeolites. (b) UV-vis spectra of Fe-MFI, FeN-MFI, and FeC-MFI zeolites. (c) Schematic illustration of incorporation of Fe sites into the Fe-MFI zeolite framework using ferrous gluconate.

indicating the Fe species are highly dispersed within the MFI zeolite.<sup>53</sup> The coordination environment of Fe species in the siliceous zeolite framework is characterized by UV-vis diffuse reflectance spectroscopy (Figure 1b). The strong intense bands at 208 and 253 nm are assigned to the charge transfer of the  $p\pi-d\pi$  transition between oxygen and iron atoms into the framework of all Fe-based zeolites, suggesting the tetrahedrally coordinated Fe sites incorporated into the Fe-MFI zeolite framework. In addition, the bands at 373 and 445 nm ascribed to iron oxide nanoparticles and bulk iron oxide particles, respectively, can be observed over the FeN-MFI and FeC-MFI zeolites.<sup>48,53,54</sup> However, no oligomeric iron oxide clusters and nanoparticles can be detected on Fe-MFI zeolite, probably because the ferrous gluconate maintains high solubility and stability under alkaline synthesis conditions (Figure 1c).

To make clear the role of ferrous gluconate during the crystallization process, the Fe-MFI zeolites crystallized at different periods (24, 36, and 72 h) were synthesized and characterized. The powder XRD patterns indicate that all the zeolites possess typical diffraction peaks for MFI structure at the crystallization periods of 24, 36, and 72 h (Figure 2a). The scanning electron microscope (SEM) images reveal that the Fe-MFI zeolites have similar morphology at the crystallization periods of 24, 36, and 72 h, which consist of uniform spherical morphology ( $\sim 200$  nm) in Figure 2d–f. The TG/DTA analysis of the uncalcined silicalite-1 zeolite exhibits two kinds of weight loss at 30–250 and 350–420 °C, respectively, which can be attributed to the removal of water adsorbed on the zeolite surface and the thermal decomposition of TPAOH in the zeolite channel (Figure 2b). However, an extra weight loss step at 450–500 °C can be detected over the uncalcined Fe-MFI zeolite at the crystallization periods of 24, 36, and 72 h, which should be due to the decomposition of  $\text{Fe}(\text{C}_6\text{H}_{12}\text{O}_7)_2$  precursors.<sup>55,56</sup> The FT-IR spectra of silicalite-1 and Fe-MFI zeolites at different crystallization periods of 24, 36, and 72 h are shown in Figure 2c. These zeolites show similar characteristic vibration bands at around 445 (T–O bond), 549 (double ring vibration), 796 (external symmetric stretch),

and 1224  $\text{cm}^{-1}$  (between  $\text{TO}_4$  tetrahedral). However, the iron-free silicalite-1 zeolite shows a band at 1108  $\text{cm}^{-1}$  attributed to the asymmetric stretching of T–O–T bonds within the silicalite-1 zeolite framework.<sup>48</sup> As for Fe-MFI at the different crystallization periods of 24, 36, and 72 h, the asymmetric stretching of the T–O–T bonds shifts to a lower frequency ( $\sim 1100$   $\text{cm}^{-1}$ ). This shift can be explained because the distance of Fe–O bonds (1.8 Å) is longer than that of Si–O bonds (1.6 Å), indicating Fe atoms are introduced into the MFI zeolite framework.<sup>41,57</sup> The Fe-MFI zeolite crystallized at 72 h is further characterized by  $\text{C}_s$ -HAADF-STEM, revealing a well-crystallized MFI characteristic structure. Noticeably, no iron oxide clusters or nanoparticles can be detected on the Fe-MFI zeolite (Figure 2g and 2h). The Fe atoms are distributed homogeneously throughout the Fe-MFI zeolite as determined by EDS elemental mapping images (Figure 2i). The above results reveal that the ferrous gluconate participates synchronously in the whole crystallization process and promotes Fe site embedding into the siliceous zeolite framework.

Fe-MFI zeolites with different Fe contents were synthesized and characterized in detail to investigate the interactions between Fe atoms and the MFI siliceous zeolite framework. The microstructures and textural properties of Fe-MFI zeolites with different Fe contents are characterized by  $\text{N}_2$  sorption technique (Table S1). The Fe-MFI zeolites exhibit a high specific surface area (423–451  $\text{m}^2 \text{g}^{-1}$ ) and a large pore volume (0.227–0.288  $\text{cm}^3 \text{g}^{-1}$ ). The UV-vis spectra of all Fe-MFI zeolites exhibit strong bands at 208 and 253 nm, indicating the tetrahedrally coordinated Fe atoms are successfully incorporated into the MFI siliceous zeolite framework.<sup>48,53</sup> However, a weak band of oligomeric Fe clusters (373 nm) can be observed when Fe content increased to 3.2%, suggesting the formation of iron oxide nanoparticles in the 3.2%Fe-MFI zeolite. It can be inferred that using ferrous gluconate can effectively embed Fe sites into the Fe-MFI zeolite framework at Fe content  $\leq 1.8\%$  (Figure 3a). The chemical properties of Fe sites in Fe-MFI were further analyzed by XPS (Figure 3b); all the Fe-MFI zeolites show two broad peaks located at about 711.3 and 724.8 eV, corresponding to Fe 2 $p_{3/2}$  and Fe 2 $p_{1/2}$ , respectively. Noticeably, the peaks of Fe 2 $p_{3/2}$  and Fe 2 $p_{1/2}$  in Fe-MFI shift to higher binding energy as compared to pure iron oxide (Fe 2 $p_{3/2}$  peak of 710.8 eV and Fe 2 $p_{1/2}$  peak of 724.2 eV), which may be attributed to the electron transfer interaction between Fe and Si atoms in the zeolite framework.<sup>58</sup> Furthermore, the reducing properties of 1.0%Fe/ $\text{SiO}_2$  and Fe-MFI zeolites with different Fe contents are measured by  $\text{H}_2$ -TPR (Figure 3c). The 1.0%Fe/ $\text{SiO}_2$  shows two obvious peaks at 351 and 429 °C, respectively, which can be assigned to the reduction of  $\text{Fe}^{3+}$  to  $\text{Fe}^{2+}$  and  $\text{Fe}^{2+}$  to Fe.<sup>26,59</sup> However, no  $\text{H}_2$  consumption peaks can be observed over the  $\text{H}_2$ -TPR spectra over all Fe-MFI zeolites due to the fact that the Fe sites embedded into the zeolite framework are hard to reduce. This indicates that the interactions between Fe sites and zeolite framework in Fe-MFI are much stronger than that in the Fe/ $\text{SiO}_2$  sample. The enhanced interactions between Fe sites and the zeolite framework might contribute to the catalytic performance of the Fe-MFI zeolite.<sup>23,33,60</sup>

Figure 3d displays the hydroxyl stretching region DRIFTS spectra of Fe-MFI zeolites with different Fe contents. All Fe-MFI zeolites show two broad peaks at  $\sim 3724$  and  $3510$   $\text{cm}^{-1}$ , assigned to the isolated terminal silanol (Si–OH) and silanol nests, respectively. Besides, a weak peak at  $3630$   $\text{cm}^{-1}$  can be



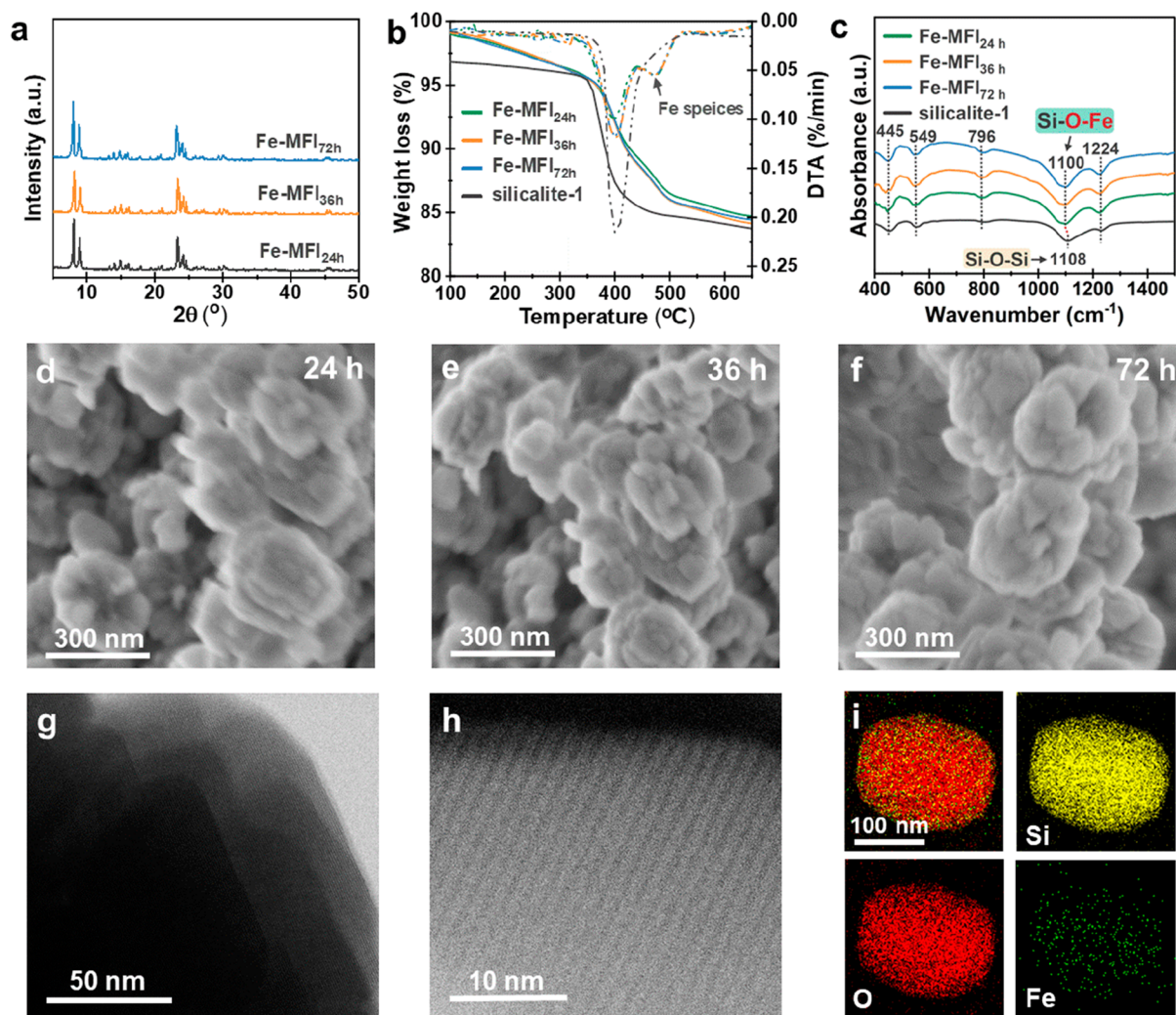


**Figure 2.** (a) XRD patterns of Fe-MFI zeolites at crystallization periods of 24, 36, and 72 h. (b) TG/DTA curves of the uncalcined silicalite-1 and Fe-MFI zeolites at the crystallization periods of 24, 36, and 72 h. (c) FTIR spectra of silicalite-1 and Fe-MFI zeolites at different crystallization periods of 24, 36, and 72 h. (d, e, f) SEM images of Fe-MFI zeolites at the crystallization periods of 24, 36, and 72 h. (g)  $C_s$ -corrected TEM and (h) HAADF-STEM images of the Fe-MFI zeolite crystallized at 72 h. (i) EDS elemental mapping images of Fe-MFI zeolite crystallized at 72 h (Si, O, and Fe).

observed over these spectra, which can be attributed to the Brønsted acid hydroxyl groups bridging between Si and Fe framework atoms in the form Fe(OH)Si bonds.<sup>61,62</sup> Noticeably, the intensities of these two peaks ( $\sim 3724$  and  $3510\text{ cm}^{-1}$ ) gradually decrease with increasing Fe contents, suggesting that the isolated silanol groups and silanol nests decrease with increasing Fe contents. In contrast, the peak at  $3630\text{ cm}^{-1}$  increases with Fe contents, indicating that the Brønsted acid bridging hydroxyl groups increase with the Fe contents. The acidic properties of the Fe-MFI zeolites are measured by  $\text{NH}_3$ -TPD and Py-FTIR. As shown in Figure 3e, all the Fe-MFI zeolites exhibit obvious  $\text{NH}_3$  desorption peaks at the temperature of  $100\text{--}400^\circ\text{C}$ . The peak below  $300^\circ\text{C}$  is probably caused by the desorption of ammonia on the weak acid sites. The  $\text{NH}_3$  desorption peak at the temperature above  $300^\circ\text{C}$  can be assigned to the ammonia adsorbed on the strong acid sites.<sup>22</sup> The  $\text{NH}_3$  desorption amounts of Fe-MFI increase significantly when the Fe content is below 1.8%. However, further increasing the Fe content to 3.2% in Fe-MFI zeolite would lead to a small increase in the  $\text{NH}_3$  desorption

amounts. Concretely, the total acid amounts in 1.0%Fe-MFI, 1.8%Fe-MFI, and 3.2%Fe-MFI, quantified by the desorbed  $\text{NH}_3$  are 0.114, 0.208, and 0.232 mmol/g, respectively (Table S1). This finding also accords with the UV-vis results, which suggest that some iron oxide nanoparticles are dispersed within the 3.2%Fe-MFI zeolite. Py-FTIR tests are applied to further identify the Lewis and Brønsted acid sites of Fe-MFI zeolites in Figure 3f. All Fe-MFI zeolites exhibit two peaks at 1450 and  $1611\text{ cm}^{-1}$ , typical for Lewis acid sites. In addition, the peak at  $1546\text{ cm}^{-1}$  is attributed to the Brønsted acid sites, and the peak at  $1490\text{ cm}^{-1}$  is assigned to both Lewis and Brønsted acid sites.<sup>55,56,60</sup> According to the above results, it is evident that the Fe sites embedded into the siliceous zeolite framework generate both Lewis and Brønsted acid sites in Fe-MFI zeolite.

The catalytic activities of Fe-MFI zeolites for propane dehydrogenation to propylene are tested (Figure 4a). Among the Fe-MFI samples, the 1.0%Fe-MFI zeolite exhibits a propane conversion of 13.5% and propylene selectivity of 90.5% for the reaction of 45 h, showing good catalytic performance in propane dehydrogenation. After incorporating

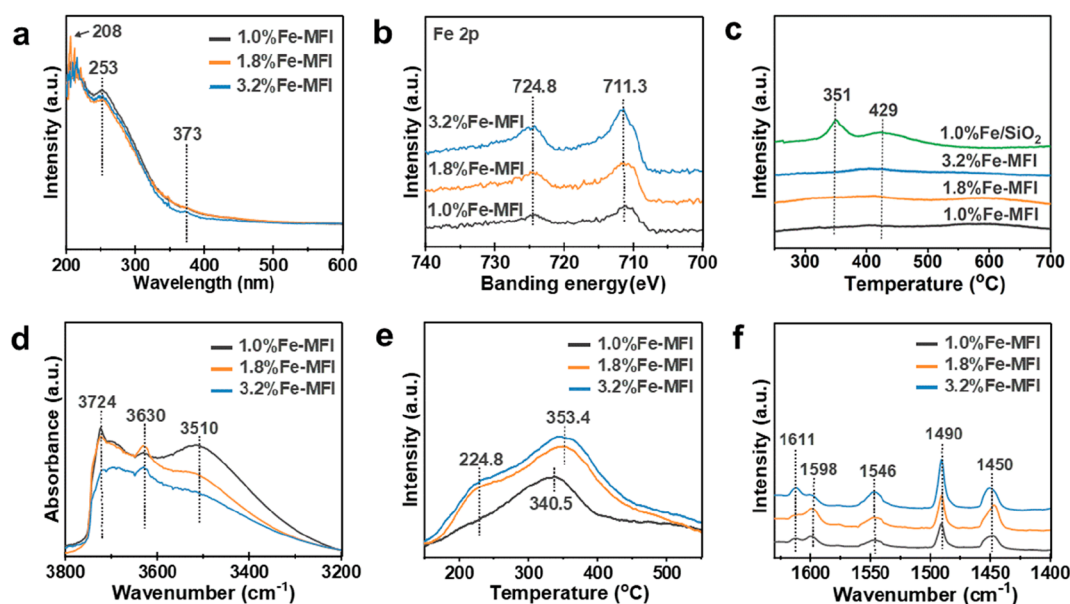


**Figure 3.** (a) UV-vis spectra of 1.0%Fe-MFI, 1.8%Fe-MFI, and 3.2%Fe-MFI zeolites. (b) Fe 2p XPS spectra of 1.0%Fe-MFI, 1.8%Fe-MFI, and 3.2%Fe-MFI zeolites. (c)  $\text{H}_2$ -TPR spectra of 1.0%Fe/SiO<sub>2</sub>, 1.0%Fe-MFI, 1.8%Fe-MFI, and 3.2%Fe-MFI zeolites. (d) DRIFTS spectra of 1.0%Fe-MFI, 1.8%Fe-MFI, and 3.2%Fe-MFI zeolites. (e)  $\text{NH}_3$ -TPD spectra of 1.0%Fe-MFI, 1.8%Fe-MFI, and 3.2%Fe-MFI zeolites. (f) FTIR spectra of 1.0%Fe-MFI, 1.8%Fe-MFI, and 3.2%Fe-MFI zeolites after pyridine adsorption and followed by evacuation at 100 °C.

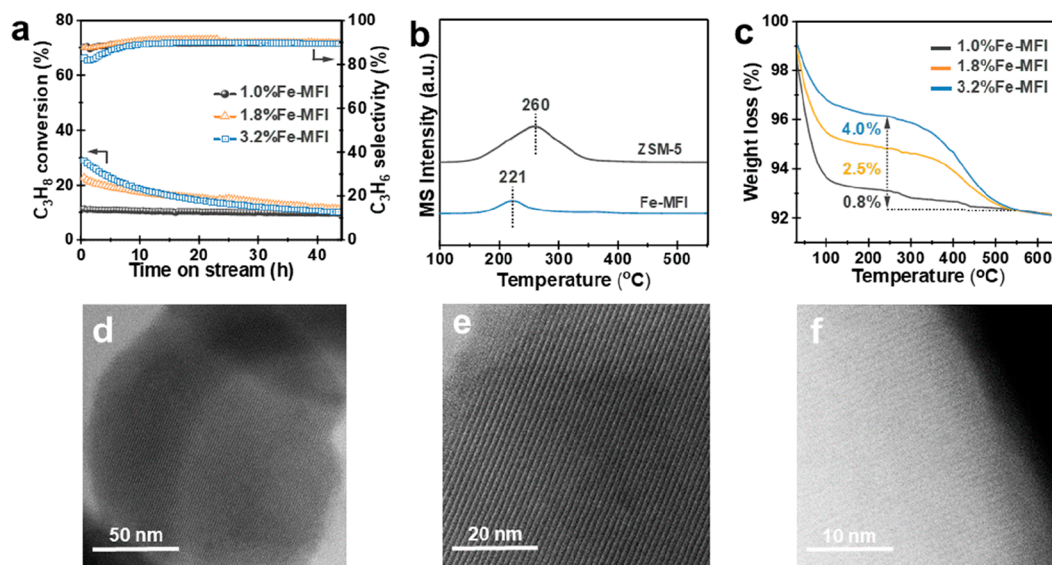


**Figure 4.** (a) Propane conversion and propylene selectivity of Fe-MFI zeolites. (b)  $\text{C}_3\text{H}_6$ -TPD/MS of Fe-MFI (Fe content of 1.8%) and ZSM-5 (Si/Al = 100) zeolites. (c) TG profiles of the used Fe-MFI zeolites at 600 °C after 45 h reaction. (d, e)  $\text{C}_s$ -corrected TEM and (f) HAADF-STEM images of used Fe-MFI (Fe content of 1.8%) after calcined for 4 h at 550 °C. Reaction conditions: 0.2 g catalysts, atmospheric pressure, 5% $\text{C}_3\text{H}_8$ /Ar, WHSV = 0.6 h<sup>-1</sup>, 600 °C.

Fe content of 1.8% into the zeolite framework, the propane conversion (23.6%) increases obviously, and the material retains good catalytic stability, demonstrating the number of active sites increases with the Fe content. In Figure 4b, the  $\text{C}_3\text{H}_6$ -TPD/MS desorption result of ZSM-5 shows a strong desorption peak at 260 °C, while a very weak peak can be observed over the Fe-MFI at 221 °C, suggesting the existence of weak interactions between propylene and Fe-MFI zeolite. Therefore, the generated propylene can quickly leave from the Fe-MFI zeolite and avoid secondary reactions. However, with further increase of the Fe content to 3.2%, the catalytic

performance obviously decreases with the reaction time because the presence of iron oxide nanoparticles within the 3.2%Fe-MFI zeolite triggers side reactions of aromatization and deep dehydrogenation resulting in low catalytic stability. Furthermore, the high reaction temperature would result in coke formation in the zeolite channel, which can also affect the catalytic performance.<sup>63</sup> To measure the coke amount on the surface of the spent Fe-MFI zeolites, TG analysis was performed. As shown in Figure 4c, all Fe-MFI zeolites show two kinds of weight loss at 30–200 °C and 300–500 °C, respectively, assigned to the removal of physically adsorbed



water and oxidative decomposition of the coke. The weight losses of Fe-MFI zeolites are 0.8% (1.0%Fe-MFI) and 2.5% (1.8%Fe-MFI), respectively. However, further increasing the Fe contents to 3.2% leads to an obvious increase in coke formation (4.0%) because the iron oxide nanoparticles in Fe-MFI zeolite aggravate carbon generation. To evaluate the stability of Fe sites in the Fe-MFI zeolite framework, the used Fe-MFI zeolites after different PDH reaction periods (0, 10, and 20 h) were measured by H<sub>2</sub>-TPR (Figure S1). No obvious H<sub>2</sub> consumption peaks are detected on the used Fe-MFI zeolites, similar to those of fresh Fe-MFI, indicating that the Fe sites in the zeolite framework are highly stable and cannot be reduced by H<sub>2</sub> before 700 °C. Also, the UV–vis spectra of the used Fe-MFI zeolites show no iron oxide clusters and nanoparticles (Figure S2), confirming the highly stable Fe species in Fe-MFI zeolites. Furthermore, C<sub>s</sub>-corrected TEM and HAADF-STEM images of the used Fe-MFI (Fe content of 1.8%) further confirm that no iron aggregates or nanoparticles are detected, and the crystallinity of Fe-MFI remains after 45 h of reaction (Figure 4d–f). It can be concluded that Fe-MFI of Fe contents ≤1.8% exhibits strong anticoking capability and high stability during propane dehydrogenation.

It has been reported that the type of Fe species can directly affect the catalytic activity of Fe-based zeolites.<sup>13,33,37,49</sup> However, the synthesis methods reported in the literature usually generated complex Fe species in Fe-based zeolite, resulting in low catalytic performance and serious coke deposits.<sup>46–48</sup> Herein, ferrous gluconate is used as the metal precursor for the synthesis of Fe-MFI zeolite. The investigation of Fe-MFI zeolites at different crystallization periods reveals that the ferrous gluconate participates synchronously in the whole crystallization process. UV–vis spectra and HAADF-STEM images demonstrate that the Fe sites will be selectively incorporated into the zeolite framework at Fe content ≤1.8%. XPS and H<sub>2</sub>-TPR demonstrate that the electronic properties of Fe sites are remarkably modified by the zeolite framework, resulting in the strong metal–support interactions in the Fe-MFI zeolite. Notably, the zeolite framework prevents the sintering of Fe sites and created Lewis and weak Brønsted acid sites, which play an important role in propane dehydrogenation. In particular, the C–H bond of propane can be efficiently activated by the Lewis acid sites, while the C–C bond cannot be broken by the weak Brønsted acid sites formed by Fe(OH)Si bonds. The synergistic effect of Fe sites in the zeolite framework and the surrounding microenvironment guarantees high activity and propylene selectivity for propane dehydrogenation.

## CONCLUSIONS

In this work, we demonstrate that ferrous gluconate can be used as an efficient Fe precursor to selectively embed Fe atoms into the MFI siliceous zeolite framework. Various characterizations illustrate that the ferrous gluconate possesses high solubility and good stability throughout the Fe-MFI zeolite crystallization process and prevents the Fe species from precipitation under alkaline synthesis conditions.

Characterizations with C<sub>s</sub>-corrected HAADF-STEM, UV–vis, and FTIR reveal that the Fe atoms are selectively incorporated into the MFI siliceous zeolite framework. H<sub>2</sub>-TPR and XPS results confirm Fe sites embedded into the MFI siliceous zeolite framework possess strong stability. NH<sub>3</sub>-TPD and Py-FTIR characterization indicate that Fe atoms embedded into the zeolite framework generate both Lewis

and weak Brønsted acid sites. The C–H bond of propane can be efficiently activated by the Lewis acid sites, while the C–C bond cannot be broken by weak Brønsted acid sites formed by Fe(OH)Si bonds. As a result, the 1.8%Fe-MFI exhibits high activity, propylene selectivity, and durability for propane dehydrogenation. The ferrous gluconate as a metal precursor opens an effective way to rationally synthesize Fe sites in the Fe-MFI zeolite framework. We believe that organometallic biomolecules as precursors can offer more possibilities for the preparation of other metal zeolites.

## ASSOCIATED CONTENT

### Supporting Information

The Supporting Information is available free of charge at <https://pubs.acs.org/doi/10.1021/acs.cgd.2c01479>.

Experimental information for H<sub>2</sub>-TPR and UV–vis spectra of used Fe-MFI zeolites and BET results of Fe-MFI zeolites (PDF)

## AUTHOR INFORMATION

### Corresponding Authors

**Yingxu Wei** – National Engineering Research Center of Lower-Carbon Catalysis Technology, Dalian National Laboratory for Clean Energy, iChEM (collaborative Innovation Center of Chemistry for Energy Materials), Dalian Institute of Chemical Physics, Chinese Academy of Sciences, Dalian 116023, China; State Key Laboratory of Catalysis, Dalian Institute of Chemical Physics, Chinese Academy of Sciences, Dalian 116023, China; [orcid.org/0000-0002-0412-1980](https://orcid.org/0000-0002-0412-1980); Email: [weiyx@dicp.ac.cn](mailto:weiyx@dicp.ac.cn)

**Zhongmin Liu** – School of Chemistry and Materials Science, University of Science and Technology of China, Hefei, Anhui 230026, China; National Engineering Research Center of Lower-Carbon Catalysis Technology, Dalian National Laboratory for Clean Energy, iChEM (collaborative Innovation Center of Chemistry for Energy Materials), Dalian Institute of Chemical Physics, Chinese Academy of Sciences, Dalian 116023, China; State Key Laboratory of Catalysis, Dalian Institute of Chemical Physics, Chinese Academy of Sciences, Dalian 116023, China; [orcid.org/0000-0002-7999-2940](https://orcid.org/0000-0002-7999-2940); Email: [liuzm@dicp.ac.cn](mailto:liuzm@dicp.ac.cn)

### Authors

**Xunming Su** – School of Chemistry and Materials Science, University of Science and Technology of China, Hefei, Anhui 230026, China; National Engineering Research Center of Lower-Carbon Catalysis Technology, Dalian National Laboratory for Clean Energy, iChEM (collaborative Innovation Center of Chemistry for Energy Materials), Dalian Institute of Chemical Physics, Chinese Academy of Sciences, Dalian 116023, China; State Key Laboratory of Catalysis, Dalian Institute of Chemical Physics, Chinese Academy of Sciences, Dalian 116023, China

**Zhong-Pan Hu** – National Engineering Research Center of Lower-Carbon Catalysis Technology, Dalian National Laboratory for Clean Energy, iChEM (collaborative Innovation Center of Chemistry for Energy Materials), Dalian Institute of Chemical Physics, Chinese Academy of Sciences, Dalian 116023, China; State Key Laboratory of Catalysis, Dalian Institute of Chemical Physics, Chinese Academy of Sciences, Dalian 116023, China

Jingfeng Han – National Engineering Research Center of Lower-Carbon Catalysis Technology, Dalian National Laboratory for Clean Energy, iChEM (collaborative Innovation Center of Chemistry for Energy Materials), Dalian Institute of Chemical Physics, Chinese Academy of Sciences, Dalian 116023, China; State Key Laboratory of Catalysis, Dalian Institute of Chemical Physics, Chinese Academy of Sciences, Dalian 116023, China

Complete contact information is available at:  
<https://pubs.acs.org/10.1021/acs.cgd.2c01479>

## Author Contributions

This paper contains extensive contributions from all authors.

## Notes

The authors declare no competing financial interest.

## ACKNOWLEDGMENTS

This work was supported by the National Key Research and Development Program of China (No. 2022YFE0116000), the National Natural Science Foundation of China (No. 22202193, 21991092, 21991090, 22172166, and 22288101), the Key Research Program of Frontier Sciences, CAS No. QYZDY-SSW-SC024, the China Postdoctoral Science Foundation (2019M661147), the Excellent Postdoctoral Support Program of Dalian Institute of Chemical Physics, CAS, the Excellent Research Assistant Funding Project of CAS, and the Youth Innovation Promotion Association CAS (2021182).

## REFERENCES

- (1) Ryoo, R.; Kim, J.; Jo, C.; Han, S. W.; Kim, J.-C.; Park, H.; Han, J.; Shin, H. S.; Shin, J. W. Rare-Earth-Platinum Alloy Nanoparticles in Mesoporous Zeolite for Catalysis. *Nature* **2020**, *585*, 221–224.
- (2) Chai, Y.; Wu, G.; Liu, X.; Ren, Y.; Dai, W.; Wang, C.; Xie, Z.; Guan, N.; Li, L. Acetylene-Selective Hydrogenation Catalyzed by Cationic Nickel Confined in Zeolite. *J. Am. Chem. Soc.* **2019**, *141*, 9920–9927.
- (3) Zhong, J.; Xu, Y.; Liu, Z. Heterogeneous Non-Mercury Catalysts for Acetylene Hydrochlorination: Progress, Challenges, and Opportunities. *Green Chem.* **2018**, *20*, 2412–2427.
- (4) Shan, Y.; Du, J.; Zhang, Y.; Shan, W.; Shi, X.; Yu, Y.; Zhang, R.; Meng, X.; Xiao, F.-S.; He, H. Selective Catalytic Reduction of NO<sub>x</sub> with NH<sub>3</sub>: Opportunities and Challenges of Cu-based Small-Pore Zeolites. *Natl. Sci. Rev.* **2021**, *8*, nwab010.
- (5) Grand, J.; Barrier, N.; Debost, M.; Clatworthy, E. B.; Laine, F.; Boullay, P.; Nesterenko, N.; Dath, J.-P.; Gilson, J.-P.; Mintova, S. Flexible Template-Free RHO Nanosized Zeolite for Selective CO<sub>2</sub> Adsorption. *Chem. Mater.* **2020**, *32*, 5985–5993.
- (6) Blanch-Raga, N.; Palomares, A.; Martínez-Triguero, J.; Valencia, S. Cu and Co Modified Beta Zeolite Catalysts for the Trichloroethylene Oxidation. *Appl. Catal., B* **2016**, *187*, 90–97.
- (7) Lin, S.; Zhi, Y.; Chen, W.; Li, H.; Zhang, W.; Lou, C.; Wu, X.; Zeng, S.; Xu, S.; Xiao, J.; et al. Molecular Routes of Dynamic Autocatalysis for Methanol-to-Hydrocarbons Reaction. *J. Am. Chem. Soc.* **2021**, *143*, 12038–12052.
- (8) Hu, Z.-P.; Yang, D.; Wang, Z.; Yuan, Z.-Y. State-of-the-Art Catalysts for Direct Dehydrogenation of Propane to Propylene. *Chin. J. Catal.* **2019**, *40*, 1233–1254.
- (9) Hu, Z.-P.; Wang, Y.; Yang, D.; Yuan, Z.-Y. CrO<sub>x</sub> Supported on High-Silica HZSM-5 for Propane Dehydrogenation. *J. Energy Chem.* **2020**, *47*, 225–233.
- (10) Li, C.; Ferri, P.; Paris, C.; Moliner, M.; Boronat, M.; Corma, A. Design and Synthesis of the Active Site Environment in Zeolite Catalysts for Selectively Manipulating Mechanistic Pathways. *J. Am. Chem. Soc.* **2021**, *143*, 10718–10726.
- (11) Hu, Z.-P.; Han, J.; Wei, Y.; Liu, Z. Dynamic Evolution of Zeolite Framework and Metal-Zeolite Interface. *ACS Catal.* **2022**, *12*, 5060–5076.
- (12) Sushkevich, V. L.; Palagin, D.; Ranocchiari, M.; Van Bokhoven, J. A. Selective Anaerobic Oxidation of Methane Enables Direct Synthesis of Methanol. *Science* **2017**, *356*, 523–527.
- (13) Snyder, B. E.; Vanelderen, P.; Bols, M. L.; Hallaert, S. D.; Böttger, L. H.; Ungur, L.; Pierloot, K.; Schoonheydt, R. A.; Sels, B. F.; Solomon, E. I. The Active Site of Low-Temperature Methane Hydroxylation in Iron-Containing Zeolites. *Nature* **2016**, *536*, 317–321.
- (14) Grand, J.; Talapaneni, S. N.; Vicente, A.; Fernandez, C.; Dib, E.; Aleksandrov, H. A.; Vayssilov, G. N.; Retoux, R.; Boullay, P.; Mintova, S.; et al. One-Pot Synthesis of Silanol-Free Nanosized MFI Zeolite. *Nat. Mater.* **2017**, *16*, 1010–1015.
- (15) Dubray, F.; Moldovan, S.; Kouvas, C.; Grand, J.; Aquino, C.; Barrier, N.; Gilson, J.-P.; Nesterenko, N.; Minoux, D.; Mintova, S. Direct Evidence for Single Molybdenum Atoms Incorporated in the Framework of MFI Zeolite Nanocrystals. *J. Am. Chem. Soc.* **2019**, *141*, 8689–8693.
- (16) Liu, L.; Lopez-Haro, M.; Meira, D. M.; Concepcion, P.; Calvino, J. J.; Corma, A. Regioselective Generation of Single-Site Iridium Atoms and Their Evolution into Stabilized Subnanometric Iridium Clusters in MWW Zeolite. *Angew. Chem., Int. Ed.* **2020**, *59*, 15695–15702.
- (17) Wang, C.; Xu, W.; Qin, Z.; Guo, H.; Liu, X.; Mintova, S. Highly Active Pd Containing EMT Zeolite Catalyst for Indirect Oxidative Carbonylation of Methanol to Dimethyl Carbonate. *J. Energy Chem.* **2021**, *52*, 191–201.
- (18) Yi, H.; Feng, Y.; Yu, Q.; Tang, X.; Zhang, Y.; Zhuang, R. Synthesis of Divalent Metal-Silicalite MEL Zeolites as Efficient Bi-Functional Adsorbents/Catalysts for Non-Methane Hydrocarbon in Cooking Oil Fumes Elimination. *Sep. Purif. Technol.* **2020**, *251*, 117363.
- (19) Ratnasamy, P.; Kumar, R. Ferrisilicate Analogs of Zeolites. *Catal. Today* **1991**, *9*, 329–416.
- (20) Kumar, R.; Raj, A.; Kumar, S. B.; Ratnasamy, P. Convenient Synthesis of Crystalline Microporous Transition Metal Silicates Using Complexing Agents. In *Studies in Surface Science and Catalysis* **1994**, *84*, 109–116.
- (21) Szécsényi, A. G.; Li, G.; Gascon, J.; Pidko, E. A. Mechanistic Complexity of Methane Oxidation with H<sub>2</sub>O<sub>2</sub> by Single-Site Fe/ZSM-5 Catalyst. *ACS Catal.* **2018**, *8*, 7961–7972.
- (22) Hu, Z.-P.; Chen, L.; Chen, C.; Yuan, Z.-Y. Fe/ZSM-5 Catalysts for Ammonia Decomposition to CO<sub>x</sub>-Free Hydrogen: Effect of SiO<sub>2</sub>/Al<sub>2</sub>O<sub>3</sub> Ratio. *Mol. Catal.* **2018**, *455*, 14–22.
- (23) Tan, P. Active Phase, Catalytic Activity, and Induction Period of Fe/zeolite Material in Nonoxidative Aromatization of Methane. *J. Catal.* **2016**, *338*, 21–29.
- (24) Pirutko, L.; Chernyavsky, V.; Uriarte, A.; Panov, G. Oxidation of Benzene to Phenol by Nitrous Oxide: Activity of Iron in Zeolite Matrices of Various Composition. *Appl. Catal. A-Gen* **2002**, *227*, 143–157.
- (25) Pannov, G.; Sobolev, V.; Kharitonov, A. The Role of Iron in N<sub>2</sub>O Decomposition on ZSM-5 Zeolite and Reactivity of the Surface Oxygen Formed. *J. Mol. Catal.* **1990**, *61*, 85–97.
- (26) Perathoner, S.; Pino, F.; Centi, G.; Giordano, G.; Katovic, A.; Nagy, J. Benzene Selective Oxidation with N<sub>2</sub>O on Fe/MFI Catalysts: Role of Zeolite and Iron Sites on the Deactivation Mechanism. *Top. Catal.* **2003**, *23*, 125–136.
- (27) Centi, G.; Perathoner, S.; Arrigo, R.; Giordano, G.; Katovic, A.; Pedula, V. Characterization and Reactivity of Fe-[Al, B] MFI Catalysts for Benzene Hydroxylation with N<sub>2</sub>O. *Appl. Catal. A-Gen* **2006**, *307*, 30–41.
- (28) Li, C.; Wang, G. Dehydrogenation of Light Alkanes to Mono-Olefins. *Chem. Soc. Rev.* **2021**, *50*, 4359–4381.
- (29) Monai, M.; Gambino, M.; Wannakao, S.; Weckhuysen, B. M. Propane to Olefins Tandem Catalysis: A Selective Route Towards Light Olefins Production. *Chem. Soc. Rev.* **2021**, *50*, 11503–11529.

- (30) Chen, S.; Chang, X.; Sun, G.; Zhang, T.; Xu, Y.; Wang, Y.; Pei, C.; Gong, J. Propane Dehydrogenation: Catalyst Development, New Chemistry, And Emerging Technologies. *Chem. Soc. Rev.* **2021**, *50*, 3315–3354.
- (31) Cheng, M.; Zhao, H.; Yang, J.; Zhao, J.; Yan, L.; Song, H.; Chou, L. The Catalytic Dehydrogenation of Isobutane and the Stability Enhancement over Fe Incorporated SBA-15. *Microporous Mesoporous Mater.* **2018**, *266*, 117–125.
- (32) Wang, L.-C.; Zhang, Y.; Xu, J.; Diao, W.; Karakalos, S.; Liu, B.; Song, X.; Wu, W.; He, T.; Ding, D. Non-Oxidative Dehydrogenation of Ethane to Ethylene over ZSM-5 Zeolite Supported Iron Catalysts. *Appl. Catal., B* **2019**, *256*, 117816.
- (33) Fan, L.; Cheng, D.; Chen, F.; Zhan, X. Preparation of Highly Dispersed Iron Species over ZSM-5 with Enhanced Metal-Support Interaction Through Freeze-Drying Impregnation. *Chin. J. Catal.* **2019**, *40*, 1109–1115.
- (34) Sazama, P.; Sathu, N. K.; Tabor, E.; Wichterlová, B.; Sklenák, Š.; Sobalík, Z. Structure and Critical Function of Fe and Acid Sites in Fe-ZSM-5 in Propane Oxidative Dehydrogenation with N<sub>2</sub>O and N<sub>2</sub>O Decomposition. *J. Catal.* **2013**, *299*, 188–203.
- (35) Kaucký, D.; Sobalík, Z.; Schwarze, M.; Vondrová, A.; Wichterlová, B. Effect of FeH-Zeolite Structure and Al-Lewis Sites on N<sub>2</sub>O Decomposition and NO/NO<sub>2</sub>-Assisted Reaction. *J. Catal.* **2006**, *238*, 293–300.
- (36) Bulánek, R.; Wichterlová, B.; Novoveská, K.; Kreibich, V. Oxidation of Propane with Oxygen and/or Nitrous Oxide over Fe-ZSM-5 with Low Iron Concentrations. *Appl. Catal. A-Gen.* **2004**, *264*, 13–22.
- (37) Zhang, J.; Tang, X.; Yi, H.; Yu, Q.; Zhang, Y.; Wei, J.; Yuan, Y. Synthesis, Characterization and Application of Fe-Zeolite: A review. *Appl. Catal. A-Gen.* **2022**, *630*, 118467.
- (38) Xia, H.; Hu, H.; Xu, S.; Xiao, K.; Zuo, S. Catalytic Conversion of Glucose to 5-Hydroxymethylfural over Fe/ $\beta$  Zeolites with Extra-Framework Isolated Fe Species in a Biphasic Reaction System. *Biomass Bioenerg.* **2018**, *108*, 426–432.
- (39) Chaliha, S.; Bhattacharyya, K. G. Fe(III)-, Co(II)-and Ni(II)-Impregnated MCM-41 for Wet Oxidative Destruction of 2, 4-Dichlorophenol in Water. *Catal. Today* **2009**, *141*, 225–233.
- (40) Sánchez-Velandia, J. E.; Villa, A. L. Isomerization of  $\alpha$ - and  $\beta$ -Pinene Epoxides over Fe or Cu Supported MCM-41 and SBA-15 Materials. *Appl. Catal. A-Gen.* **2019**, *580*, 17–27.
- (41) Wu, G.; Hei, F.; Guan, N.; Li, L. Oxidative Dehydrogenation of Propane with Nitrous Oxide over Fe-MFI Prepared by Ion-Exchange: Effect of Acid Post-Treatments. *Catal. Sci. Technol.* **2013**, *3*, 1333–1342.
- (42) Guzmán-Vargas, A.; Delahay, G.; Coq, B. Catalytic Decomposition of N<sub>2</sub>O and Catalytic Reduction of N<sub>2</sub>O and N<sub>2</sub>O + NO by NH<sub>3</sub> in the Presence of O<sub>2</sub> over Fe-Zeolite. *Appl. Catal., B* **2003**, *42*, 369–379.
- (43) Iwasaki, M.; Yamazaki, K.; Banno, K.; Shinjoh, H. Characterization of Fe/ZSM-5 DeNO<sub>x</sub> Catalysts Prepared by Different Methods: Relationships Between Active Fe Sites and NH<sub>3</sub>-SCR Performance. *J. Catal.* **2008**, *260*, 205–216.
- (44) Yue, Y.; Liu, H.; Yuan, P.; Yu, C.; Bao, X. One-Pot Synthesis of Hierarchical Fe-ZSM-5 Zeolites from Natural Aluminosilicates for Selective Catalytic Reduction of NO by NH<sub>3</sub>. *Sci. Rep.* **2015**, *5*, 9270.
- (45) Wu, G.; Hei, F.; Guan, N.; Li, L. Oxidative Dehydrogenation of Propane with Nitrous Oxide over Fe-MFI Prepared by Ion-Exchange: Effect of Acid Post-Treatments. *Catal. Sci. Technol.* **2013**, *3*, 1333–1342.
- (46) Yun, J. H.; Lobo, R. F. Radical Cation Intermediates in Propane Dehydrogenation and Propene Hydrogenation over H-[Fe] Zeolites. *J. Phys. Chem. C* **2014**, *118*, 27292–27300.
- (47) Yun, J. H.; Lobo, R. F. Catalytic Dehydrogenation of Propane over Iron-Silicate Zeolites. *J. Catal.* **2014**, *312*, 263–270.
- (48) Zhang, W.; Wang, B.; Rui, P.; Fan, N.; Liao, W. Hierarchical Zeolite Fe-MFI as Activity Enhanced Catalysts for Selective Liquid-Phase Dehydration of 1-Phenylethanol. *Catal. Lett.* **2021**, *151*, 2716–2723.
- (49) Yang, Z.; Li, H.; Zhou, H.; Wang, L.; Wang, L.; Zhu, Q.; Xiao, J.; Meng, X.; Chen, J.; Xiao, F.-S. Coking-Resistant Iron Catalyst in Ethane Dehydrogenation Achieved Through Siliceous Zeolite Modulation. *J. Am. Chem. Soc.* **2020**, *142*, 16429–16436.
- (50) Camacho-Bunquin, J.; Aich, P.; Ferrandon, M.; Das, U.; Dogan, F.; Curtiss, L. A.; Miller, J. T.; Marshall, C. L.; Hock, A. S.; Stair, P. C.; Getsoian, A. Single-Site Zinc on Silica Catalysts for Propylene Hydrogenation and Propane Dehydrogenation: Synthesis and Reactivity Evaluation Using an Integrated Atomic Layer Deposition-Catalysis Instrument. *J. Catal.* **2017**, *345*, 170–182.
- (51) Hu, B.; Schweitzer, N. M.; Zhang, G.; Kraft, S. J.; Childers, D. J.; Lanci, M. P.; Miller, J. T.; Hock, A. S. Isolated Fe<sup>II</sup> on Silica as a Selective Propane Dehydrogenation Catalyst. *ACS Catal.* **2015**, *5*, 3494–3503.
- (52) Kaphan, D. M.; Ferrandon, M. S.; Langeslay, R. R.; Celik, G.; Wegener, E. C.; Liu, C.; Niklas, J.; Poluektov, O. G.; Delferro, M. Mechanistic Aspects of a Surface Organovanadium(III) Catalyst for Hydrocarbon Hydrogenation and Dehydrogenation. *ACS Catal.* **2019**, *9*, 11055–11066.
- (53) Kumar, M. S.; Schwidder, M.; Grünert, W.; Brückner, A. On the Nature of Different Iron Sites and Their Catalytic Role in Fe-ZSM-5 DeNO<sub>x</sub> Catalysts: New Insights by a Combined EPR and UV-vis Spectroscopic Approach. *J. Catal.* **2004**, *227*, 384–397.
- (54) Bordiga, S.; Buzzoni, R.; Geobaldo, F.; Lamberti, C.; Giamello, E.; Zecchina, A.; Leofanti, G.; Petrini, G.; Tozzola, G.; Vlaic, G. Structure and Reactivity of Framework and Extraframework Iron in Fe-silicalite as Investigated by Spectroscopic and Physicochemical Methods. *J. Catal.* **1996**, *158*, 486–501.
- (55) Su, X.; Hu, Z.-P.; Han, J.; Jia, Y.; Xu, S.; Zhang, J.; Fan, D.; Wei, Y.; Liu, Z. Biomolecule-Inspired Synthesis of Framework Zinc in MFI zeolite for Propane Dehydrogenation. *Microporous Mesoporous Mater.* **2023**, *348*, 112371.
- (56) Sun, Q.; Wang, N.; Fan, Q.; Zeng, L.; Mayoral, A.; Miao, S.; Yang, R.; Jiang, Z.; Zhou, Y. J.; et al. Subnanometer Bimetallic Platinum-Zinc Clusters in Zeolites for Propane Dehydrogenation. *Angew. Chem.* **2020**, *132*, 19618–19627.
- (57) Borade, R. Synthesis and Characterization of Ferrisilicate Zeolite of Pentasil Group. *Zeolites* **1987**, *7*, 398–403.
- (58) Kuivila, C.; Butt, J.; Stair, P. Characterization of Surface Species on Iron Synthesis Catalysts by X-ray Photoelectron Spectroscopy. *Appl. Surf. Sci.* **1988**, *32*, 99–121.
- (59) Naumann d'Alnoncourt, R.; Friedrich, M.; Kunkes, E.; Rosenthal, D.; Girgsdies, F.; Zhang, B.; Shao, L.; Schuster, M.; Behrens, M.; Schlögl, R. Strong Metal-Support Interactions Between Palladium and Iron Oxide and Their Effect on CO Oxidation. *J. Catal.* **2014**, *317*, 220–228.
- (60) Hu, Z.-P.; Qin, G.; Han, J.; Zhang, W.; Wang, N.; Zheng, Y.; Jiang, Q.; Ji, T.; Yuan, Z.-Y.; Xiao, J.; Wei, Y.; Liu, Z. Atomic Insight into the Local Structure and Microenvironment of Isolated Co-Motifs in MFI Zeolite Frameworks for Propane Dehydrogenation. *J. Am. Chem. Soc.* **2022**, *144*, 12127–12137.
- (61) Konnov, S. V.; Dubray, F.; Clatworthy, E. B.; Kouvasas, C.; Gilson, J. P.; Dath, J. P.; Minoux, D.; Aquino, C.; Valtchev, V.; Moldovan, S.; Koneti, S.; Nesterenko, N.; Mintova, S. Novel Strategy for the Synthesis of Ultra-Stable Single-Site Mo-ZSM-5 Zeolite Nanocrystals. *Angew. Chem., Int. Ed.* **2020**, *132*, 19721–19728.
- (62) Medeiros-Costa, I. C.; Dib, E.; Dubray, F.; Moldovan, S.; Gilson, J.-P.; Dath, J.-P.; Nesterenko, N.; Aleksandrov, H. A.; Vayssilov, G. N.; Mintova, S. Unraveling the Effect of Silanol Defects on the Insertion of Single-Site Mo in the MFI Zeolite Framework. *Inorg. Chem.* **2022**, *61*, 1418–1425.
- (63) Sahoo, S. K.; Rao, P.; Rajeshwer, D.; Krishnamurthy, K. R.; Singh, I. D. Structural Characterization of Coke Deposits on Industrial Spent Paraffin Dehydrogenation Catalysts. *Appl. Catal. A-Gen.* **2003**, *244*, 311–321.